

Solving Multivariable Equations with Tandem Metamaterial Kernels

Qingze Tan^{1, 2, 3}, Chao Qian^{1, 2, 3, *}, Tong Cai^{1, 2, 3},
Bin Zheng^{1, 2, 3}, and Hongsheng Chen^{1, 2, 3, *}

Abstract—A fundamental building block in characterizing and tackling scientific and industrial questions boils down to the ability of quickly solving mathematical equations. However, with the ever-growing volume of information and unsustainable integration growth in electronic processors, a radically new modality for solving equations is highly imminent. Here, we introduce an electromagnetic counterpart to solve multivariable complex equations, where two metamaterial kernels are connected in series to form a closed-loop electromagnetic system. Complex valued information is carried by electromagnetic fields, and the equation solution for arbitrary input signals can be recursively attained after a number of feedbacks. As an illustration, we present the capability of such a system in solving eight complex equations, and inversely design two 4×4 metamaterial kernels by topology optimization, whose average element error is reduced to smaller than 10^{-4} . Having accomplished all unknown coefficients with high fidelity, our work represents a conspicuous apparatus for a myriad of enticing applications in ultracompact signal processing and neuromorphic computing.

1. INTRODUCTION

The ability of quickly processing the increasing volume of information generated every day is in ever-pressing demand over the past decades, especially with the proliferation of artificial intelligence. To meet the high demand on computing resources, we have been seeing a great evolution of electronic processors, such as graphics processing units (GPUs) and field-programmable gate arrays (FPGAs) for scenario-specific applications. Unfortunately, the slowing down or even failure of Moore's law makes this persistent evolution become extremely difficult and thus in turn intensifies the contradiction between supply and demand [1]. Specifically, the speed and energy of electronic processor are hindered from the approach of physical limit in semiconductor technology, posing an obstacle to further lift parasitic capacitance and clock rate. In this context, it is highly anticipated to exploit a radically new computing modality to be complementary with electronic processors and to find some on-demand applications in which new computing modality is the greatest.

Optical computing, which operates with photons instead of electrons, has been found to be an alternative paradigm to overcome the inherent limitation of electronics [2–7]. Whereas electronic computing currently dominates the computing community, we cannot underestimate the unique advantages brought by optical computing in the near future, notably with the twilight of Moore's law. The unique advantages are mainly manifested by the speed-of-light operation, paralleling process, and low power consumption. As early as 1980s, researchers have managed to exploit optical analogy computing using a bulky system of lenses and filter [8, 9]. Recent advances in metamaterials offer a versatile and miniaturized platform to enable a myriad of functional processor for specialized tasks, such

Received 6 June 2022, Accepted 7 September 2022, Scheduled 15 October 2022

* Corresponding author: Hongsheng Chen (hansomchen@zju.edu.cn), Chao Qian (chaoq@intl.zju.edu.cn).

¹ ZJU-UIUC Institute, Interdisciplinary Center for Quantum Information, State Key Laboratory of Modern Optical Instrumentation, Zhejiang University, Hangzhou 310027, China. ² ZJU-Hangzhou Global Science and Technology Innovation Center, Key Lab. of Advanced Micro/Nano Electronic Devices & Smart Systems of Zhejiang, Zhejiang University, Hangzhou 310027, China. ³ Jinhua Institute of Zhejiang University, Zhejiang University, Jinhua 321099, China.

as spatial differentiation, logic operation, and optical neural network [10–31]. Apart from that, the fast promotion of optical computing is also inseparable from the assistance of many advanced optimization algorithms [32, 33]. Researchers are now attempting to bring optical computing into some real-world applications involving high-throughput and low-latency data processing [34–36].

As a fundamental building block, equation solving plays an important role in analyzing, modeling, and characterizing scientific and industrial questions. However, the related studies for electromagnetic implementation are relatively few. More recent works have presented an original and fresh approach to create wave-based integral equation solver and have been well recognized [37, 38]. It processes the integral equation into discrete format and then designs a compact computing kernel to physically characterize the given integral equation. By connecting the output waveguides to the input waveguides of the computing kernel, the equation solution can be attained in steady state through hundreds of electromagnetic wave circulations in the system. Based on this, solving a set of equations is still in high demand but challenging, most notably those with a large number of the variables. This is mostly because the difficulty of obtaining an accurate and small-footprint computing kernel with target large-scale scattering matrix is increased significantly.

In this work, we design a compact electromagnetic device to solve a set of linear equations, where two inhomogeneous metamaterial kernels are connected to construct a closed-loop system. Complex-valued information is carried by electromagnetic fields, and the solution for arbitrary input signals can be attained in the steady state after a number of cycles in the closed-loop system. The metamaterial kernels are strongly designed with topology optimization, whose average element error (AEE) is reduced to 10^{-4} . For a given high-dimensional equation, we decompose it into two low-dimensional matrices, which is mimicked by the scattering matrices of two metamaterial kernels. As a proof-of-concept, we demonstrate the capability of such a system in solving eight complex equations. Our work fills the gap about electromagnetic equation solver and holds great potential to extend the frontiers in integrated computing photonic circuitry, fast analog signal processing, and optical neural network [25–38].

2. RESULTS

2.1. Architecture of Electromagnetic Mathematic Equation Solver

For a set of linear nonhomogeneous equations $\mathbf{A}\mathbf{X} = \mathbf{B}$, the solution can be generally summarized as $\mathbf{A}^{-1}\mathbf{B}$, as sketched in Fig. 1(a). In this process, the key step boils down to the deduction of the inverse of the coefficient matrix \mathbf{A} , whose complexity scale is proportional to $O(2N)^3$, and $2N$ is the dimension of \mathbf{A} . Fig. 1(b) shows the conceptual representation of our electromagnetic equation solver, where two metamaterial kernels are connected in series to form a closed-loop system. The transmission matrix of each metamaterial structure imitates the coefficient matrix of equations. For example, \mathbf{X}_1 will become $\mathbf{A}_1\mathbf{X}_1$ after passing through the metamaterial kernel. After a number of feedbacks, the system will reach a steady state (the running time is negligible). Thus, the general relation governing the loop system follows,

$$\begin{cases} \mathbf{A}_1\mathbf{X}_1 + \mathbf{B}_1 = \mathbf{X}_2 \\ \mathbf{A}_2\mathbf{X}_2 + \mathbf{B}_2 = \mathbf{X}_1 \end{cases} \quad (1)$$

where $[\mathbf{X}_1, \mathbf{X}_2]$ represents the $2N \times 1$ vectorial solution obtained as the complex-valued signal carried by electromagnetic waves; $[\mathbf{B}_1, \mathbf{B}_2]$ represents the $2N \times 1$ vector input signal; \mathbf{A}_1 and \mathbf{A}_2 are two $N \times N$ transmission matrices of the operational kernel (the left inset in Fig. 1(b)). We further simplify Eq. (1) into the matrix form,

$$\begin{bmatrix} -\mathbf{A}_{1,N \times N}, \mathbf{I}_{N \times N} \\ \mathbf{I}_{N \times N}, -\mathbf{A}_{2,N \times N} \end{bmatrix} \cdot \begin{bmatrix} \mathbf{X}_{1,N \times 1} \\ \mathbf{X}_{2,N \times 1} \end{bmatrix} = \begin{bmatrix} \mathbf{B}_{1,N \times 1} \\ \mathbf{B}_{2,N \times 1} \end{bmatrix} \quad (2)$$

where \mathbf{I} is an unit matrix. Comparing Eq. (2) with Fig. 1(a), their mathematical forms are equivalent. Assuming that $\mathbf{A}_1 = -\mathbf{A}_{11}$, $\mathbf{A}_2 = -\mathbf{A}_{22}$, $\mathbf{I} = \mathbf{A}_{12} = \mathbf{A}_{21}$, the two formulas are exactly the same. Although the unit matrix enforcement on \mathbf{A}_{12} and \mathbf{A}_{21} makes the electromagnetic implementation lose some generalizations, it is still very useful, especially in the applications based on state transition. Therefore, for a given mathematical equation set, we first decompose the coefficient matrix $\mathbf{A}_{2N \times 2N}$ into two matrices $\mathbf{A}_{1,N \times N}$ and $\mathbf{A}_{2,N \times N}$, and then set up the whole electromagnetic platform with tandem metamaterial kernels and input/output components.

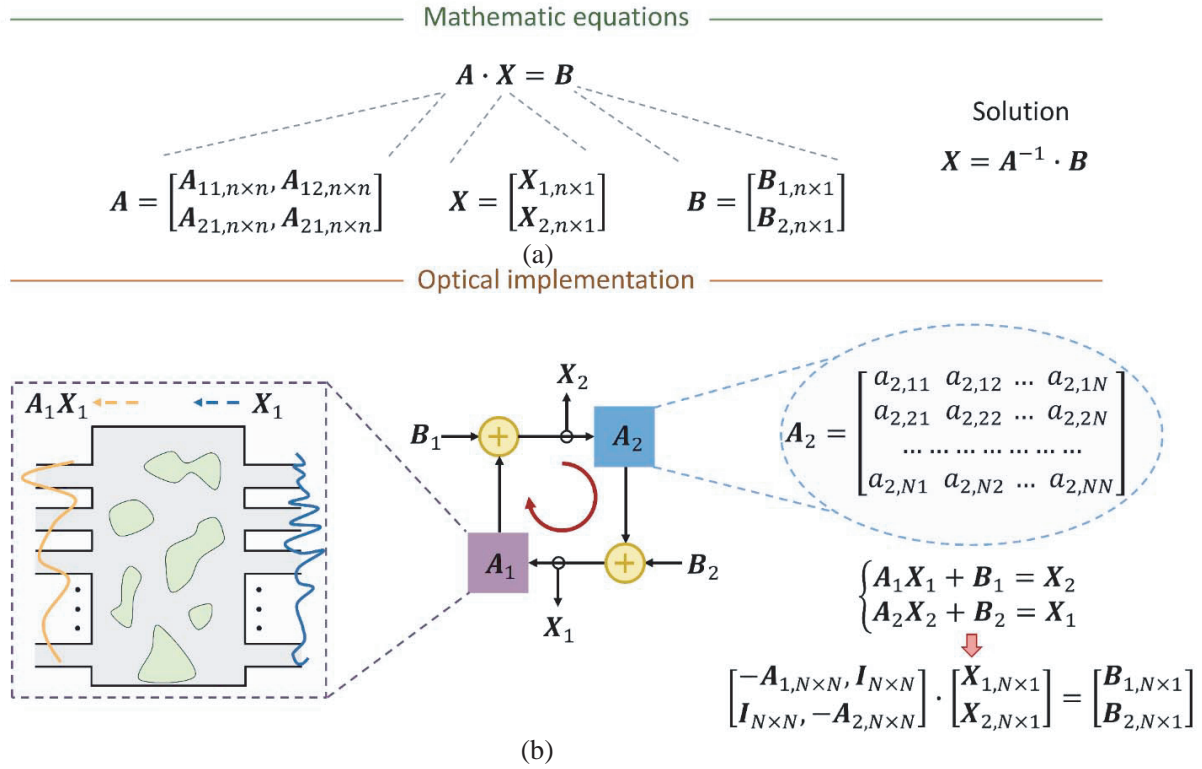


Figure 1. Schematic of electromagnetic implementation for solving multivariable mathematical equations. (a) Equation solving in mathematics. For a non-singular coefficient matrix \mathbf{A} , the mathematical solution can be expressed as the product of \mathbf{A}^{-1} and \mathbf{B} , i.e., $\mathbf{X} = \mathbf{A}^{-1}\mathbf{B}$. In other words, we can also decompose these matrices into block matrices. (b) Electromagnetic implementation of equation solver. Two metamaterial kernels are connected in series to form a closed-loop network, each of which is inversely designed to characterize the coefficient matrix \mathbf{A}_1 and \mathbf{A}_2 with high fidelity. The coefficient matrix is embodied as the transmission matrix in this case. For a customer-defined input \mathbf{B}_1 and \mathbf{B}_2 , the tandem metamaterial system will reach a steady-state after a number of recursive wave propagations. Finally, we extract the equation solution from \mathbf{X}_1 and \mathbf{X}_2 .

2.2. Inverse Design of Metamaterial Kernel

The task is now reduced to finding two computational kernels whose transmission matrices \mathbf{A}_1 and \mathbf{A}_2 are the same as the coefficient matrices $-\mathbf{A}_{11}$ and $-\mathbf{A}_{22}$. As shown in Fig. 2(a), the physical layout of the computational kernel consists of a two-dimensional (2D) domain sandwiched by planar metallic waveguides (the spatial parameters are shown in Fig. S1 in Supporting Information). The top and bottom sides are surrounded by electromagnetic absorber. We consider the fundamental TE_{10} mode to carry information, and the operating frequency is selected as $f = 5 \text{ GHz}$ (the wavelength $\lambda = 6 \text{ cm}$). Four inputs (rectangular waveguides) and four outputs are attached to the left and right sides, so the transmission matrix of the computational kernel is a 4×4 matrix. In addition, there is also a 4×4 reflection matrix, which shall be miniaturized to zero. The center green highlighted region is the designed region ($30 \text{ cm} \times 48 \text{ cm}$, $5\lambda \times 8\lambda$), where the dielectric distribution associated with the expected transmission matrix needs to be found during optimization.

The electromagnetic optimization that finds the dielectric distribution associated with the transmission matrix of the operational kernel was undertaken using the topological optimization method [33, 38]. Topological optimization can produce optimized dielectric distribution without any constraint on geometrical shapes. This is different from deep learning assisted inverse design, in which one always needs to discretize the electromagnetic devices with fixed square, circular shape and more;

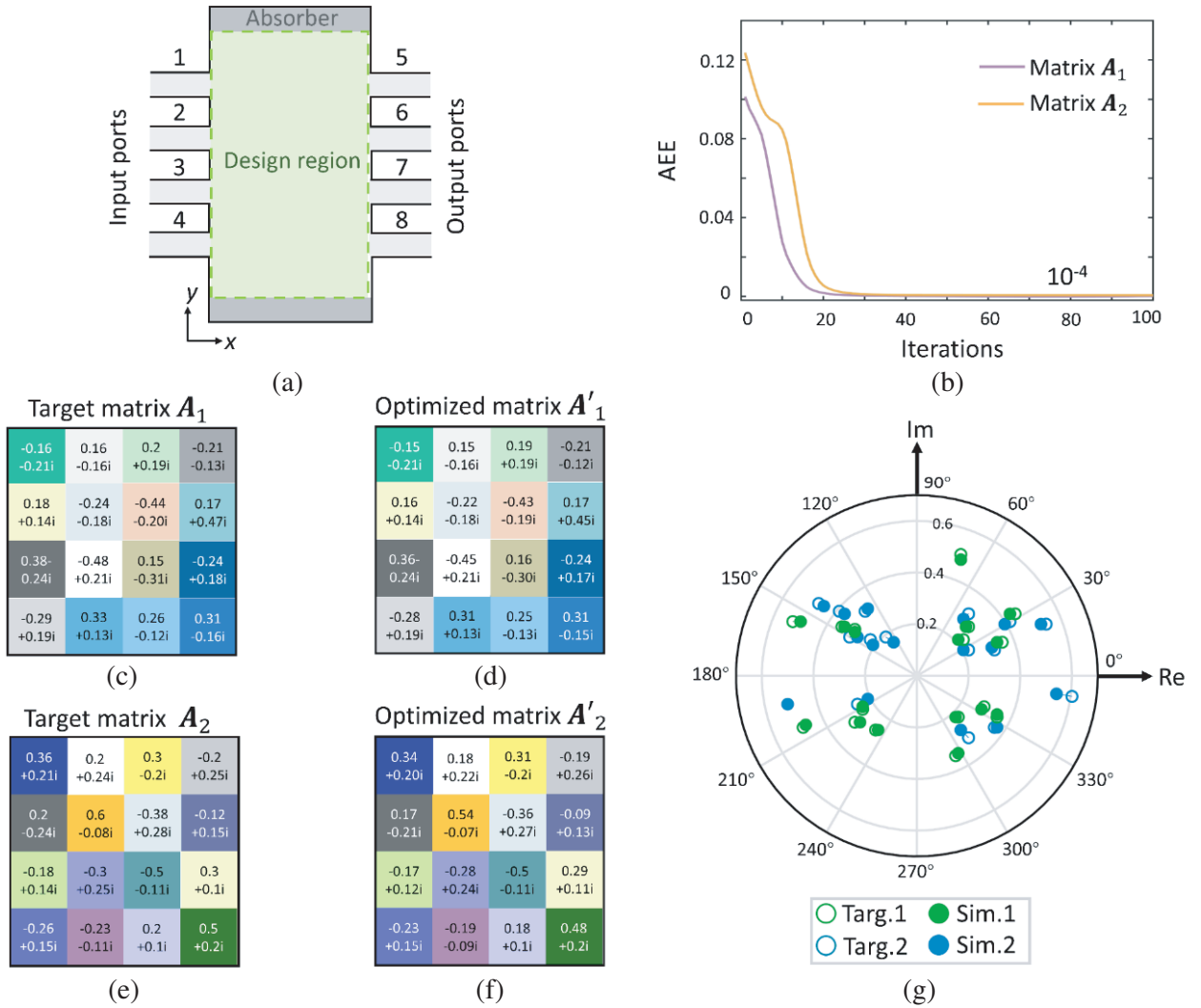


Figure 2. Inverse design of metamaterial kernels with topology optimization. (a) Inhomogeneous metamaterial kernel to mimic the coefficient matrix. It contains four input waveguides and four output waveguides on either side of the design region; see the geometric parameters in Fig. S1. The design region is surrounded by absorbing boundary layer on top and bottom. The inverse design aims to optimize the spatial inhomogeneity in the design region with topology optimization. (b) The AEE over iterations. (c)–(f) Target matrix and the optimized matrix enabled by the designed metamaterial kernels. (g) Comparison between the optimized results (solid circle) and the corresponding target matrix (hollow circle).

the optimized outcome is generated from one combination of these pixels and looks very rigid. To facilitate the topology optimization process, we deploy a loss function AEE defined as the complex-plane “distance” between the S parameters (i.e., transmission matrices A'_1 and A'_2) and their expected values (i.e., target matrices A_1 and A_2). The optimization goal was to minimize the AEE and the reflection matrix of the computational kernel (ideally, to be zero). The optimized variable is defined by the relative permittivity at each point, which is bounded between air with the relative permittivity of 1 and Rexolite, a low-loss polystyrene with the relative permittivity of 2.53. Following a satisfactory convergence, the next step of optimization was performed using penalty function to enforce the relative permittivity binarize as air or Rexolite; see the iterative process of binaryzation in Fig. S2 in Supporting Information. At last, the optimization is ceased when a satisfactory small error in the binarized structure is reached.

2.3. Numerical Simulation

We randomly select two target matrices and optimize the computational kernels with topology optimization, as shown in Fig. 2. After dozens of iterations, convergence is obtained, and the AEE is decreased to 10^{-4} , suggesting that the two computational kernels can implement the target stochastic matrix with negligible errors (Fig. 2(b)). To intuitively illustrate the accuracy, we plot the ideal matrices (hollow circles) and the optimized matrices (solid circles) of the two computational kernels in Fig. 2(g). The high consistence indicates that the metamaterial structure can accurately perform desired complex-valued matrix as operational kernel for the equation solver. In Supporting Information (Figs. S3 and S4), we simulate the computational kernels with fabrication errors, which exhibit a good tolerance.

Figures 3(a), (c) display the binary distribution consisting of either air or the commercially available dielectric material Rexolite, where Rexolite is represented in green. The electric field distributions with different inputs are plotted in Figs. 3(b), (d), providing visual confirmation for optimization results enabled by the computational kernels. We observe that the reflection waves of scattering matrices are nearly zero, which is crucial to the electromagnetic equation solver. And each figure represents one column of the optimized matrices presented in Figs. 2(d), (f). The electric field distributions and the target stochastic matrices are well matched. From the physical view, we have realized the precise control of the amplitude and phase of electromagnetic field in this compact computational kernel. Next, we will build the complete metamaterial system of equation solver by utilizing these two well-designed kernels.

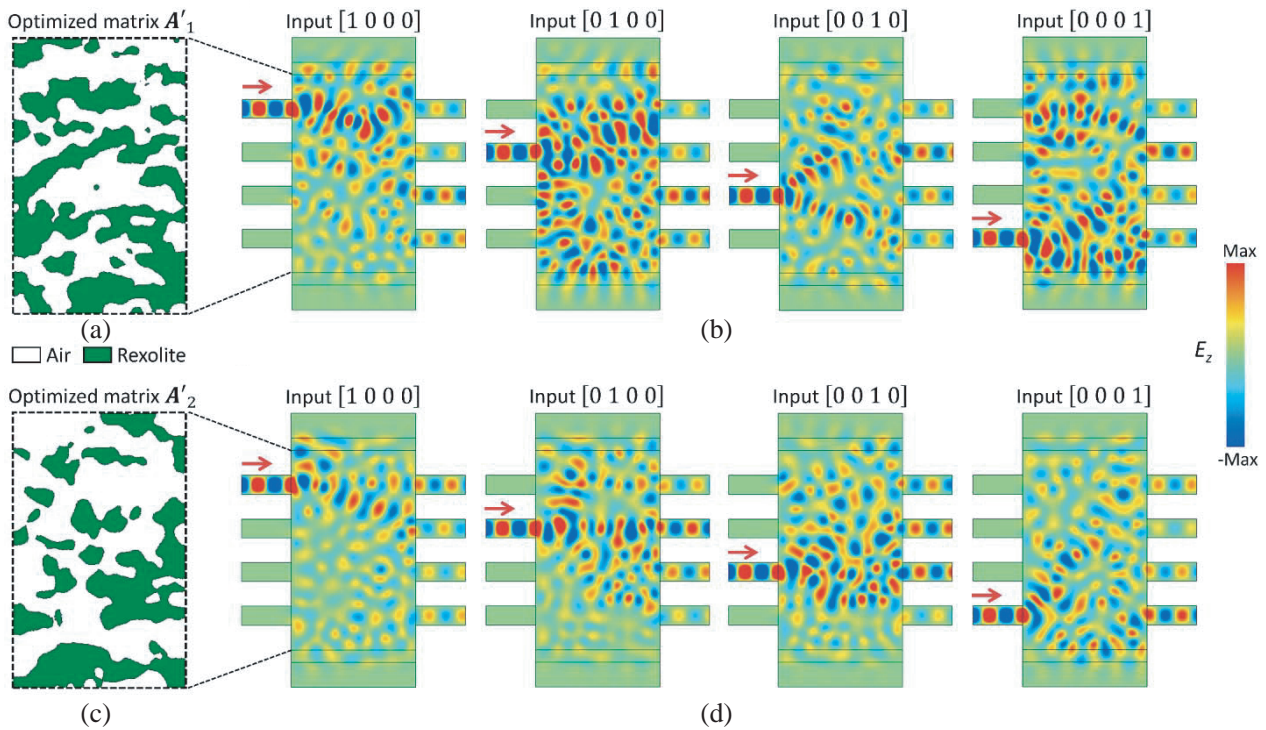


Figure 3. Numerical results of metamaterial kernels. (a), (c) Inhomogeneous distributions of the relative permittivity inside the metamaterial kernels. The metamaterial kernels are composed of either air or the commercially available dielectric material Rexolite with the relative permittivity of 2.53. (b), (d) Electrical field distributions inside the metamaterial kernels with different inputs. Four input waveguides are excited one-by-one. For all cases, almost no reflected waves go back to the inputs.

2.4. Solving Multivariable Equations

Fig. 4(a) illustrates the numerical simulation result for the distribution of E_z field (snapshot in time) in the assembled closed-loop system; see Supplementary Movie 1. It mainly includes two well-designed

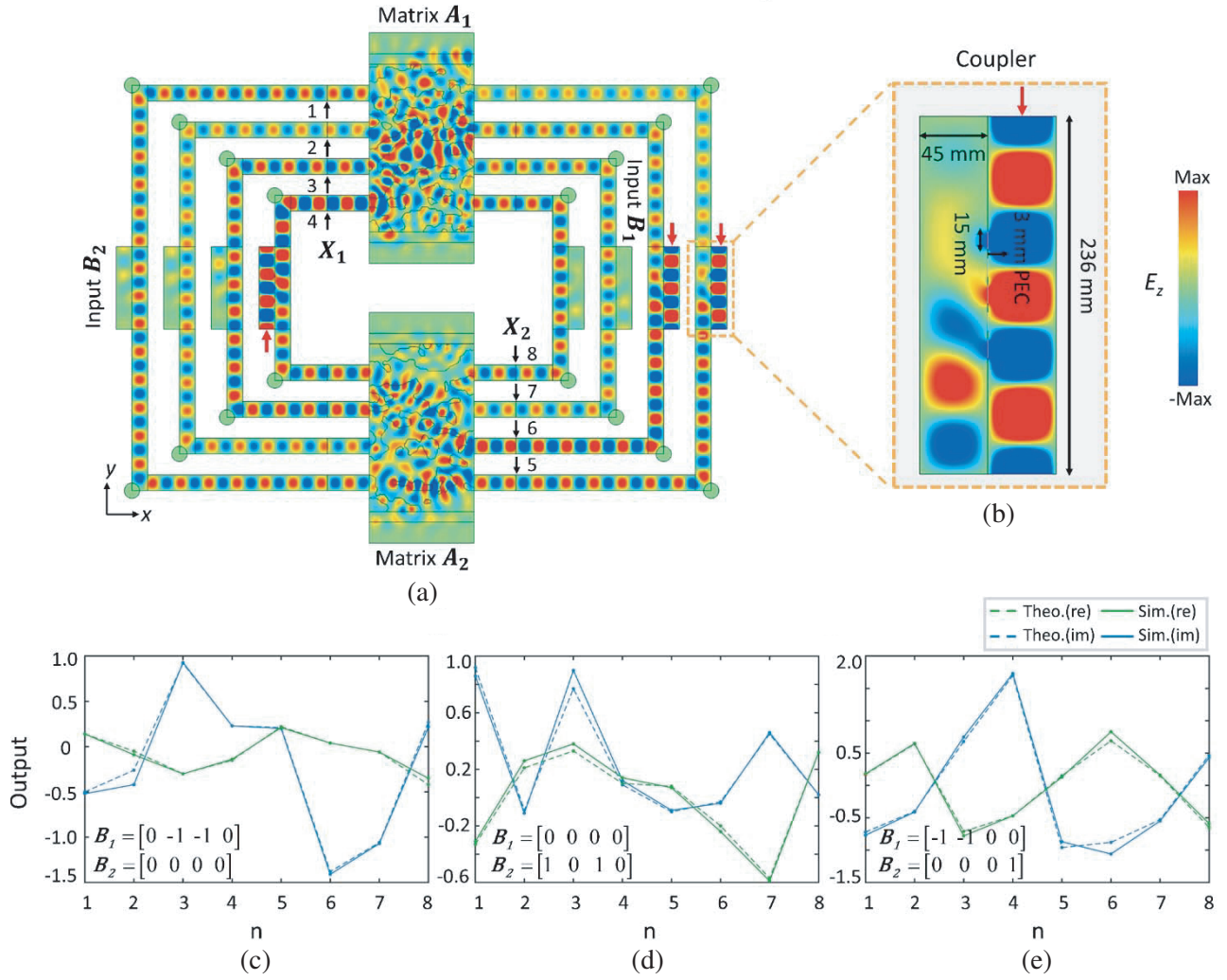


Figure 4. Solving multivariable equations with tandem metamaterial kernels. (a) Electric field distribution in the closed-loop network. The two metamaterial kernels are connected through four waveguides. The electrical lengths of all waveguides connecting the kernel to couplers are multiples of the TE_{10} guide wavelength, ensuring zero phase difference between the two ends of each waveguide. (b) Electric field distribution of the directional coupler. The red arrow shows the excited port. The coupling efficiency of this coupler is 11.3%, the reflection and transmission phase of the coupler is also set to be zero. (c)–(e) Solution of equations carried by electromagnetic waves for three representative input patterns (insets). The solutions by optics (solid lines) are consistent with the theoretical results (dashed lines), in term of both real and imaginary parts.

computational kernels, four waveguides, and directional couplers shown in Fig. 4(b). The directional couplers are also designed at the operating frequency to create 11.3% power coupling efficiency with zero reflection. The transmission phase of the coupler is also set to zero. This is a crucial consideration to eliminate the effect of the presence of coupler in the signal path. Fig. 4(b) shows the simulation results of the electric field distribution in the coupler, consisting of two parallel waveguides with perfect electric conductor (PEC) walls, each with the width of 45 mm same as the connecting waveguide in system. There are five openings (15 mm) in the common PEC wall between the waveguides in order to couple a portion of the power between the two waveguides. The distance between the two adjacent openings is 3 mm. This coupler is symmetric, and the scattering matrix follows the general format. The electrical lengths of all waveguides connecting operational kernels and couplers are multiples of the TE_{10} guide

wavelength, ensuring zero phase difference between the two ends of each waveguide. The system can be excited at arbitrary waveguide (through the corresponding coupler) with a monochromatic signal with electric field. The complex values of the field distribution constructed on the waveguides (at the position of small black vertical arrows in Fig. 4(a)) represents the solution of the corresponding input. The input signal $[\mathbf{B}_1, \mathbf{B}_2]$ may be an arbitrary complex distribution of monochromatic waves at the eight input ports. Fig. 4(a) shows the steady-state simulated result when three input ports are excited, as indicated by red arrows.

The complex-valued fields on the output ports of eight couplers are then used to extract the solutions of the equation (the specific method is shown in Supporting Information), which are shown in Figs. 4(c)–(e) containing 3 representative input patterns (more results can be found in Figs. S5 and S6 in Supporting Information). Compared with the ideal theoretical results (dashed lines), we attain an excellent agreement between theoretical and simulated results. The small deviations may be attributed to the errors generated during binarization process and the influence of embedding coupler. We also simulated the equation-solver system constructed by the other two metamaterial kernels shown in Fig. S7 in Supporting Information, and the corresponding results are presented in Fig. S8. These results strongly verify the capability of such a system to solve multivariable equations. Furthermore, we see that the effect caused by the loss of employed material is negligible, and the designed equation-solver is robust to the noises of the input signals (Figs. S9 and S10 in Supporting Information).

3. CONCLUSION

In conclusion, we have proposed a tandem metamaterial system to solve multivariable mathematical equations. The tandem metamaterial kernels are inversely designed to make their transmission matrix consistent with the coefficient matrix of the equation. We employ topology optimization to design the metamaterial structure without any geometric constrains and explicitly impose realistic dielectric parameter to ensure that the electromagnetic solver could be easily fabricated. Taking a set of eight linear equations as a demonstration, we first decompose it into two 4×4 metamaterial kernels to significantly decrease the design complexity. The two designed metamaterial kernels are designed to have only a small-scale footprint whose size is $5\lambda \times 8\lambda$, and the AEE loss is decreased to 10^{-4} . On this foundation, we cascade the two metamaterial kernels with four waveguides to successfully solve the equations with high accuracy. Although the equation solver was demonstrated in the microwave, the concept is relevant and can be readily generalized to other high frequencies with a similar framework (Fig. S11 in Supporting Information).

Our work opens a new avenue for solving large-scale mathematical equations in optics. Moving forward, it would be also interesting to enable a re-programmable optical solver by incorporating active components and nonlinear materials into metamaterials kernels, behaving as the analogue, wave-based counterpart of electronic field-programmable gate arrays [10]. Whereas the metamaterials kernels are iteratively optimized beforehand on computer, we can even apply in-situ training on the integrated photonics platform [39], in conjunction with reinforcement learning and other heuristic algorithms [14]. We anticipate that this formalism may be carried over to other enticing applications in on-chip signal processing and neuromorphic computing to drastically reduce their footprints without compromising the efficiency or functionality [40, 41].

ACKNOWLEDGMENT

This work at Zhejiang University was sponsored by the National Natural Science Foundation of China (NNSFC) under grant Nos. 61625502, 11961141010, 61975176, 62071424, and 62101485, the Top-Notch Young Talents Program of China, and the Fundamental Research Funds for the Central Universities.

REFERENCES

1. Waldrop, M. M., “The chips are down for Moore’s law,” *Nature*, Vol. 530, 144–147, 2016.
2. Solli, D. R. and B. Jalali, “Analog optical computing,” *Nat. Photon.*, Vol. 9, 704–706, 2015.

3. Lee, S. H., “Optical analog solutions of partial differential and integral equations,” *Opt. Eng.*, Vol. 24, 240141, 1985.
4. Ferrera, M., Y. Park, L. Razzari, B. E. Little, S. T. Chu, R. Morandotti, D. J. Moss, and J. Azaña, “On-chip CMOS-compatible all-optical integrator,” *Nat. Commun.*, Vol. 1, 1–5, 2010.
5. Rajbenbach, H., Y. Fainman, and S. H. Lee, “Optical implementation of an iterative algorithm for matrix inversion,” *Appl. Opt.*, Vol. 26, 1024–1031, 1987.
6. Wu, K., C. Soci, P. P. Shum, and N. I. Zheludev, “Computing matrix inversion with optical networks,” *Opt. Express*, Vol. 22, 295–304, 2014.
7. Cederquist, J., “Integral-equation solution using coherent optical feedback,” *J. Opt. Soc. Am.*, Vol. 71, 651–655, 1981.
8. Cederquist, J. and S. H. Lee, “Coherent optical feedback for the analog solution of partial differential equations,” *J. Opt. Soc. Am.*, Vol. 70, 944–953, 1980.
9. Leger, J. R. and S. H. Lee, “Coherent optical implementation of generalized two-dimensional transforms,” *Opt. Eng.*, Vol. 18, 185518, 1979.
10. Qian, C., B. Zheng, Y. Shen, L. Jing, E. Li, L. Shen, and H. Chen, “Deep-learning-enabled self-adaptive microwave cloak without human intervention,” *Nat. Photon.*, Vol. 14, 383–390, 2020.
11. Gong, D., T. Ma, J. Evans, and S. He, “Deep neural networks for image super-resolution in optical microscopy by using modified hybrid task cascade U-net,” *Progress In Electromagnetics Research*, Vol. 171, 185–199, 2021.
12. Chen, X., Z. Wei, M. Li, and P. Rocca, “A review of deep learning approaches for inverse scattering problems,” *Progress In Electromagnetics Research*, Vol. 167, 67–81, 2020.
13. Zhen, Z., C. Qian, Y. Jia, Z. Fan, R. Hao, T. Cai, B. Zheng, H. Chen, and E. Li, “Realizing transmitted metasurface cloak by a tandem neural network,” *Photon. Res.*, Vol. 9, B229–B235, 2021.
14. Qian, C. and H. Chen, “A perspective on the next generation of invisibility cloaks — Intelligent cloaks,” *Appl. Phys. Lett.*, Vol. 118, 180501, 2021.
15. Hua, Y., C. Qian, H. Chen, and H. Wang, “Experimental topology-optimized cloak for water waves,” *Mater. Today Phys.*, Vol. 27, 100754, 2022.
16. Fan, Z., C. Qian, Y. Jia, Z. Wang, Y. Ding, D. Wang, L. Tian, E. Li, T. Cai, B. Zheng, I. Kaminer, and H. Chen, “Homeostatic neuro-metasurfaces for dynamic wireless channel management,” *Sci. Adv.*, Vol. 8, eabn7905, 2022.
17. Tan, Q., B. Zheng, T. Cai, C. Qian, R. Zhu, X. Li, and H. Chen, “Broadband spin-locked metasurface retroreflector,” *Adv. Sci.*, Vol. 2201397, 1–7, 2022.
18. Qian, C., Z. Wang, H. Qian, T. Cai, B. Zheng, X. Lin, Y. Shen, I. Kaminer, E. Li, and H. Chen, “Dynamic recognition and mirage using neuro-metamaterials,” *Nat. Commun.*, Vol. 13, 2694, 2022.
19. Cai, T., S. Tang, B. Zheng, G. Wang, W. Ji, C. Qian, Z. Wang, E. Li, and H. Chen, “Ultrawideband chromatic aberration-free meta-mirrors,” *Adv. Photon.*, Vol. 3, 016001, 2021.
20. Qian, C., Y. Yang, Y. Hua, C. Wang, X. Lin, T. Cai, D. Ye, E. Li, I. Kaminer, and H. Chen, “Breaking the fundamental scattering limit with gain metasurfaces,” *Nat. Commun.*, Vol. 13, 4383, 2022.
21. Zhang, J., C. Qian, Z. Fan, J. Chen, E. Li, J. Jin, and H. Chen, “Heterogeneous transfer-learning-enabled diverse metasurface design,” *Adv. Opt. Mater.*, Vol. 2200748, 1–9, 2022.
22. Jia, Y., C. Qian, Z. Fan, Y. Ding, Z. Wang, D. Wang, E. Li, B. Zheng, T. Cai, and H. Chen, “In-situ customized illusion enabled by global metasurface reconstruction,” *Adv. Funct. Mater.*, Vol. 32, 2109331, 2022.
23. Hu, Z., N. He, Y. Sun, Y. Jin, and S. He, “Wideband high-reflection chiral dielectric metasurface,” *Progress In Electromagnetics Research*, Vol. 172, 51–60, 2021.
24. Wu, N., Y. Zhang, H. Ma, H. Chen, and H. Qian, “Tunable high-Q plasmonic metasurface with multiple surface lattice resonances,” *Progress In Electromagnetics Research*, Vol. 172, 23–32, 2021.
25. Khoram, E., A. Chen, D. Liu, L. Ying, Q. Wang, M. Yuan, and Z. Yu, “Nanophotonic media for artificial neural inference,” *Photon. Res.*, Vol. 7, 823–827, 2019.

26. Wang, Z., C. Qian, T. Cai, L. Tian, Z. Fan, J. Liu, Y. Shen, L. Jing, J. Jin, E. Li, B. Zheng, and H. Chen, "Demonstration of spider-eyes-like intelligent antennas for dynamically perceiving incoming waves," *Adv. Intell. Syst.*, Vol. 3, 2100066, 2021.
27. Qian, C., X. Lin, X. Lin, J. Xu, Y. Sun, E. Li, B. Zhang, and H. Chen, "Performing optical logic operations by a diffractive neural network," *Light Sci. Appl.*, Vol. 9, 59, 2020.
28. Zhou, Y., H. Zheng, I. I. Kravchenko, and J. Valentine, "Flat optics for image differentiation," *Nat. Photon.*, Vol. 14, 316–323, 2020.
29. Kwon, H., D. Sounas, A. Cordaro, A. Polman, and A. Alù, "Nonlocal metasurfaces for optical signal processing," *Phys. Rev. Lett.*, Vol. 121, 173004, 2018.
30. Cordaro, A., H. Kwon, D. Sounas, A. F. Koenderink, A. Alù, and A. Polman, "High-index dielectric metasurfaces performing mathematical operations," *Nano Lett.*, Vol. 19, 8418–8423, 2019.
31. Silva, A., F. Monticone, G. Castaldi, V. Galdi, A. Alù, and N. Engheta, "Performing mathematical operations with metamaterials," *Science*, Vol. 343, 160–163, 2014.
32. Su, L., A. Y. Piggott, N. V. Sapra, J. Petykiewicz, and J. Vučković, "Inverse design and demonstration of a compact on-chip narrowband three-channel wavelength demultiplexer," *ACS Photon.*, Vol. 5, 301–305, 2017.
33. Jensen, J. S. and O. Sigmund, "Topology optimization for nano-photonics," *Laser Photonics Rev.*, Vol. 5, 308–321, 2011.
34. Qu, Y., H. Zhu, Y. Shen, J. Zhang, C. Tao, P. Ghosh, and M. Qiu, "Inverse design of an integrated-nanophotonics optical neural network," *Sci. Bull.*, Vol. 65, 1177–1183, 2020.
35. Hughes, T. W., I. A. D. Williamson, M. Minkov, and S. Fan, "Wave physics as analog recurrent neural network," *Sci. Adv.*, Vol. 5, eaay6946, 2019.
36. Harris, N. C., J. Carolan, D. Bunandar, M. Prabhu, M. Hochberg, T. Baehr-Jones, M. L. Fanto, A. M. Smith, C. C. Tison, P. M. Alsing, and, D. Englund "Linear programmable nanophotonic processors," *Optica*, Vol. 5, 1623, 2018.
37. Estakhri, N. M., B. Edwards, and N. Engheta, "Inverse-designed metastructures that solve equations," *Science*, Vol. 363, 1333–1338, 2019.
38. Camacho, M., B. Edwards, and N. Engheta, "A single inverse-designed photonic structure that performs parallel computing," *Nat. Commun.*, Vol. 12, 1466, 2021.
39. Hughes, T. W., M. Minkov, Y. Shi, and S. Fan, "Training of photonic neural networks through in situ backpropagation and gradient measurement," *Optica*, Vol. 5, 864–871, 2018.
40. Beneck, R. J., A. Das, G. Mackertich-Sengerdy, R. J. Chaky, Y. Wu, S. Soltani, and D. Werner, "Reconfigurable antennas: A review of recent progress and future prospects for next generation," *Progress In Electromagnetics Research*, Vol. 171, 89–121, 2021.
41. Zhou, H., J. Dong, J. Cheng, W. Dong, C. Huang, Y. Shen, Q. Zhang, M. Gu, C. Qian, H. Chen, Z. Ruan, and X. Zhang, "Photonic matrix multiplication lights up photonic accelerator and beyond," *Light Sci. Appl.*, Vol. 11, No. 2, 158–178, 2022.